Non-uniform distribution of dendritic nonlinearities differentially engages thalamostriatal and corticostriatal inputs onto cholinergic interneurons

Abbreviated title: Dendritic nonlinearities in striatal cholinergic interneurons

Osnat Oz[1], Lior Matityahu[1], Aviv Mizrahi-Kliger[1,2], Alexander Kaplan[1,2], Noa Berkowitz[1], Lior Tiroshi[1†], Hagai Bergman[1,2,3], Joshua A. Goldberg[1*]

[1]Department of Medical Neurobiology, Institute of Medical Research Israel – Canada, The Faculty of Medicine,
[2]Edmond and Lily Safra Center for Brain Sciences,
The Hebrew University of Jerusalem, 9112102 Jerusalem, Israel
[3]Department of Neurosurgery, Hadassah Medical Center, 9112102 Jerusalem, Israel

[†]Current address: Department of Neurobiology, Northwestern University, Evanston, IL, 60208, USA

[*]Corresponding author, joshua.goldberg2@mail.huji.ac.il

Abstract

The tonic activity of striatal cholinergic interneurons (CINs) is modified differentially by their afferent inputs. Although their unitary synaptic currents are identical, cortical inputs onto distal dendrites only weakly entrain CINs, whereas proximal thalamic inputs trigger abrupt pauses in discharge in response to salient external stimuli. To test whether the dendritic expression of the active conductances that drive autonomous discharge contribute to the CINs' capacity to dissociate cortical from thalamic inputs, we used an optogenetics-based method to quantify dendritic excitability. We found that the persistent sodium (NaP) current gave rise to dendritic boosting and that the hyperpolarization-activated cyclic nucleotide-gated (HCN) current gave rise to a subhertz membrane resonance. This resonance may underlie our novel finding of an association between CIN pauses and internally-generated slow wave events in sleeping non-human primates. Moreover, our method indicated that dendritic NaP and HCN currents were preferentially expressed in proximal dendrites. We validated this non-uniform distribution with two-photon imaging of dendritic back-propagating action potentials, and by demonstrating boosting of thalamic, but not cortical, inputs by NaP currents. Thus, the localization of active dendritic conductances in CIN dendrites mirrors the spatial distribution of afferent terminals and may promote their differential responses to thalamic vs. cortical inputs.

Introduction

The striatal cholinergic interneuron (CIN) is a key modulator of the striatal microcircuitry, impacting the neuronal excitability, synaptic transmission and synaptic plasticity of spiny projection neurons (SPNs), as well as other striatal interneurons (Abudukeyoumu et al., 2019; Assous, 2021; Goldberg et al., 2012). There are two processes that drive the ongoing release of acetylcholine (ACh) by CINs. First, the two glutamatergic inputs arising from cerebral cortex and intralaminar nuclei of the thalamus can drive CINs to discharge (Bradfield et al., 2013; Ding et al., 2010; Doig et al., 2014; Kosillo et al., 2016; Lapper and Bolam, 1992; Matsumoto et al., 2001; Sharott et al., 2012; Thomas et al., 2000). While the unitary synaptic currents generated by these two inputs in CINs are identical (Aceves Buendia et al., 2019), that thalamic inputs to CINs dominate in the sense that they that give rise to larger excitatory post-synaptic potentials (EPSPs) in acute striatal slices (Johansson and Silberberg, 2020) and can trigger abrupt pause responses, often flanked by excitatory peaks, to external saliency-related cues (Apicella et al., 1991; Goldberg and Reynolds, 2011; Graybiel et al., 1994; Kimura et al., 1984; Matsumoto et al., 2001; Morris et al., 2004; Raz et al., 1996). In contrast, cortical inputs to CINs are weaker in that, in acute striatal slices, they give rise to smaller EPSPs and cannot trigger the pause response (Ding et al., 2010), although, these differences are less pronounced in intact animals (Doig et al., 2014).

Second, even in the absence of afferent input, CINs exhibit multiple autonomously generated discharge patterns – including regular and irregular pacemaking, as well as burst firing (Bennett et al., 2000; Bennett and Wilson, 1999; Goldberg and Reynolds, 2011; Goldberg and Wilson, 2010). These firing patterns are generated by an interplay between various nonlinear ionic currents including voltage- and calcium-activated K^+ currents, as well as two voltage-dependent pacemaker currents: the hyperpolarization-activated cyclic nucleotide-gated (HCN) current; and the persistent Na^+ (NaP) current (Bennett et al., 2000; Deng et al., 2007; Goldberg et al., 2009; Goldberg and Wilson, 2010, 2005; McGuirt et al., 2021; Oswald et al., 2009; Song and Surmeier, 1996; Wilson, 2005; Wilson and Goldberg, 2006). The main purpose of these pacemaker currents presumably is to guarantee the ongoing release of ACh onto the striatal microcircuitry by sustaining the autonomous discharge of CINs. Nevertheless, these pacemaker (and other subthreshold) currents will also impact how cortical and thalamic inputs are integrated by the CINs.

Attaining a mechanistic (e.g., dynamical systems) understanding of how the repertoire of CIN firing patterns is generated, requires a full characterization of the nonlinear properties of the pacemaker (and other) currents (e.g., by determining their voltage dependence and kinetics) – which is a daunting endeavor. In contrast, understanding how these currents impact synaptic inputs is a simpler task. Because individual synaptic inputs are small, the membrane nonlinearities can be *linearized* making the analysis of their impact simpler and more general - a treatment called the quasi-linear membrane approximation. This analysis dates back to Mauro (Koch, 1984; Mauro et al., 1970) and has shown that quasi-linear membranes can give rise to two qualitatively different transformations of inputs: *amplification* and *resonance* (Goldberg et al., 2007; Hutcheon and Yarom, 2000). Being a linear approximation, the quasi-linear approximation is amenable to Fourier analysis, which helps to better define these transformations as linear (time-invariant) filters on the input in frequency space.

Amplification arises from regenerative ionic currents – that provide positive feedback – including inward (depolarizing) currents activated by depolarization, such as the NaP current. Here the main effect in frequency space is amplification of the amplitude response (as compared to the response of a passive linear membrane). Resonance arises from restorative currents – that provide negative feedback – including inward currents activated by hyperpolarization, such the HCN current. In frequency space, the defining properties of resonance is a peak (at a non-zero frequency) in the amplitude response, and a zero-crossing of the phase delay (at a nearby frequency). On a practical level, the quasi-linear response properties of a membrane can be measured by providing a small-amplitude, sinusoidally-modulated voltage command to an intracellularly-recorded neuron and recording the resultant sinusoidal output current. Calculating the ratio of the voltage amplitude to the current response yields an estimate of the membrane's impedance (which is, loosely speaking, an indication of the neuron's "input resistance" to a sinusoidal input as a function of its frequency). Membrane impedances have been reported for various neuronal types in the brain (Hutcheon et al., 1996; Ulrich, 2002), including in the striatum (Beatty et al., 2015). Beatty and collaborators (2015) found that CINs exhibit a resonance in the vicinity of 1 Hz. Moreover, they found that the shape of the impedance function depended on the holding voltage, which is understandable given that the amplitude of the various subthreshold currents is voltage-dependent. Finally, with use of tetrodotoxin (TTX), a selective antagonist

100 of voltage-activated Na^+ (Nav) channels, Beatty and collaborators (2015) demonstrated that
101 NaP currents contributed to these filtering properties of the CIN membrane.

102 Use of somatic voltage perturbations, however, fails to discriminate the role played by
103 the CINs' dendritic arbor *per se* in transforming synaptic inputs. The CINs' dendritic arbor
104 can span well over half a millimeter from the soma (Wilson, 2004), with cortical inputs
105 terminating on distal dendrites and thalamic inputs terminating perisomatically and on
106 proximal dendrites (Doig et al., 2014; Lapper and Bolam, 1992; Thomas et al., 2000). Both
107 dendritic morphology (as taught by cable theory) and dendritic nonlinearities will lead to
108 distal cortical inputs being integrated differently from proximal thalamic input. Thus, the
109 impact of membrane nonlinearities on the quasi-linear approximation will depend on *where*
110 they are expressed throughout the dendritic arbor. To address this question, we recently
111 developed an optogenetics-based experimental method (that relies on the use of quasi-linear
112 cable theory and Fourier analysis) to determine the duration of the delays introduced by
113 dendrites, and how these delays impact the rapidity and fidelity of a neuron's response to its
114 input. We used our method to study GABAergic neurons of the substantia nigra pars
115 reticulata (SNr) that expressed channelrhodopsin-2 (ChR2). We illuminated (with a 470 nm
116 LED) either a small perisomatic region or the entire dendritic arbor. Comparison of the two
117 illumination regimes enabled us to demonstrate that dendrites (that in the SNr can be >700
118 μm long) introduce a significant integration delay. The analysis also yielded that SNr
119 dendrites behaved like passive linear filters, without evidence for amplification or
120 resonances, or any dependence on holding voltage (Tiroshi and Goldberg, 2019).

121 In the present study, we apply our method to study nonlinearities of CIN dendrites.
122 We demonstrate that HCN and NaP currents shape the quasi-linear response properties of
123 CINs, and that their presence in the dendrites contributes additional phase delays.
124 Furthermore, we show that our analysis can reveal information about dendritic location of
125 membrane nonlinearities, and use the analysis to deduce that both HCN and NaP currents are
126 expressed primarily proximally. The proximal distribution of NaP currents is supported by
127 measuring: a) how far autonomously generated backpropagating action potentials (bAPs)
128 actively invade the dendritic arbor; and b) the differential boosting by NaP currents of
129 proximal thalamostriatal vs. distal corticostriatal EPSPs.

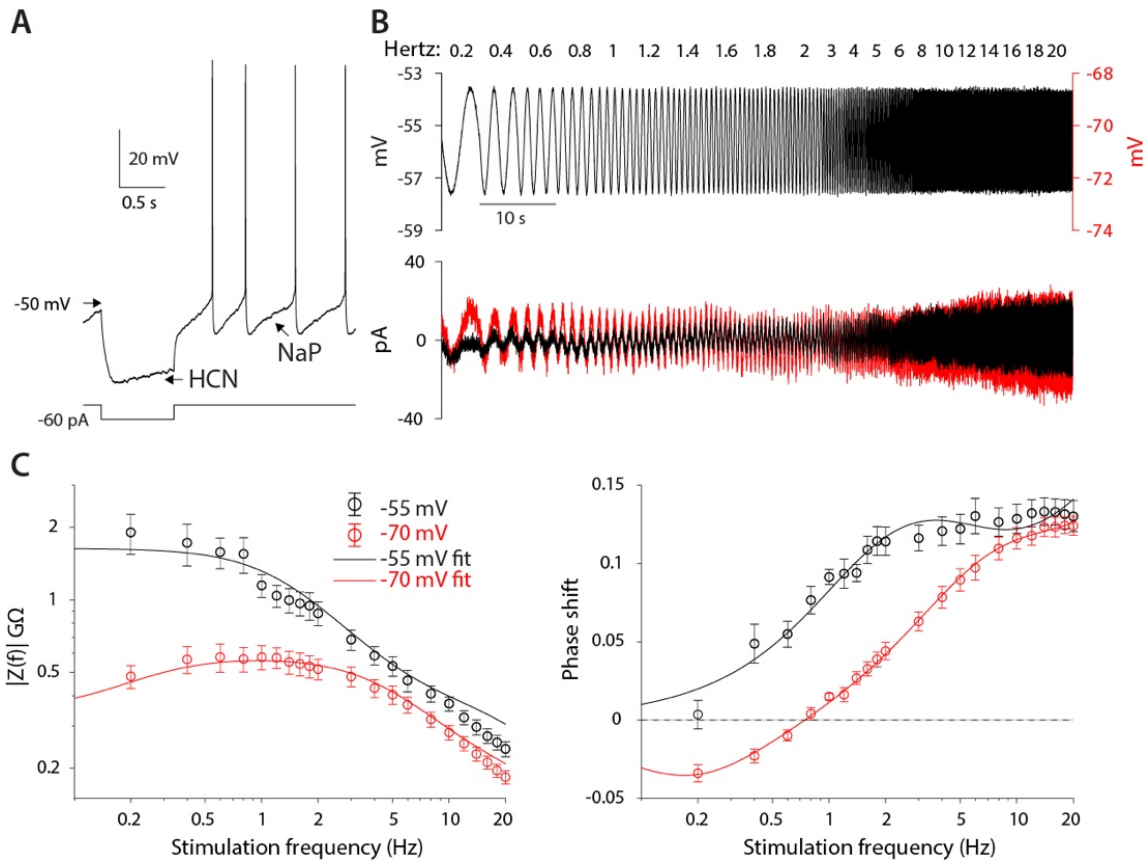

Figure 1: CIN membranes exhibit voltage-dependent quasi-linear properties. **A.** CINs exhibit a voltage sag due to HCN currents, and autonomous pacemaking due to NaP currents. **B.** Application of 2 mV sinusoidal voltage commands to the soma, of increasing frequencies, elicits a current response that is voltage dependent (black trace, –55 mV; red trace, –70 mV). **C.** Estimation of the impedance (left) and phase shift (right) show that at –55 mV, CINs exhibit an amplified impedance and that at –70 mV, CINs exhibit a resonance (non-monotonic impedance and negative phase delays). Solid lines are parameter fits for $(\alpha^2 + \beta^2)^{-1/2}$ up to a scale factor (left), and phase shift, ϕ_s (right, see Eq. 4).

Results

<u>Ionic currents underlying amplification and resonance in cholinergic interneurons</u>

The HCN and NaP currents depolarize CINs over largely non-overlapping voltage ranges. The HCN current is mostly active below –60 mV and is responsible for the voltage sag in response to a hyperpolarizing current pulse (Fig. 1A, “HCN”), whereas the NaP current takes over at –60 mV and is necessary and sufficient (Bennett et al., 2000) to drive CINs to action potential threshold (Fig. 1A, “NaP”). Therefore, because NaP is a regenerative current, while HCN is a restorative current, we would expect the current responses to an oscillating voltage command to depend strongly on whether the membrane voltage is clamped above or below –60 mV (Beatty et al., 2015). We therefore held mouse CINs in whole-cell voltage clamp (*n = 10* neurons, *N = 4* mice), first at –55 mV, and subjected them

141 to a voltage command that was composed of a continuous sequence of sinusoidal cycles with
142 an amplitude of 2 mV and a frequency that increases discretely from 0.2 to 20 Hz. The
143 current amplitude was very small at low frequencies and increased monotonically to the high
144 frequency (Fig. 1B, black), which is suggestive of an impedance curve with amplified lower
145 frequencies. Loosely speaking, this means that the CINs' "input resistance" to a low
146 frequency oscillatory input currents is boosted. As expected (Fig. 1C, black), the impedance
147 curve, $|Z(f)|$, exhibited an amplifying structure, with the phase delay being strictly positive. In
148 order to quantify the degree of amplification, we fit the model of the phase delay, ϕ_s, for an
149 iso-potential cell with quasi-linear properties (see Materials and Methods). In this fit, there is
150 a (negative) amplifying parameter, μ_n – that is derived from biophysical properties of
151 amplifying current (e.g., the slope of the activation curve, reversal potential, etc.) (Goldberg
152 et al., 2007) – which was estimated to be $\mu_n = -3.9$.

153 When neurons were held at –70 mV ($n = 10$ neurons, $N = 7$ mice), the current
154 response was very different, it was much larger at subhertz frequencies as compared to the
155 experiment at –55 mV, and then exhibited what looks like a slightly decreasing amplitude for
156 frequencies near 1 Hz, followed by an amplitude increase at higher frequencies (Fig. 1B,
157 red). Estimation of the amplitude response and phase delay (Fig. 1C, red), revealed
158 significantly different curves (amplitude: $P = 6 \cdot 10^{-25}$, phase: $P = 1 \cdot 10^{-17}$, ANCOVA) with a
159 clear resonance peak at approximately 1 Hz, and a zero crossing at a slightly lower frequency
160 (Fig. 1C, red). Fitting the somatic phase delay yielded a reasonable fit only when both an
161 amplifying and resonant component were included in the fit with the amplifying parameter
162 ($\mu_n = -3.4$) being only slightly reduced relative to the –55 mV fit. In contrast, the additional
163 (positive) resonance parameter, μ_h – which is derived from the biophysical properties of the
164 restorative current – was estimated to be $\mu_h = 1.6$ (see Materials and Methods) based on the
165 fit to the negative lobe in the phase delay.

166 The previous experiments suggest that the amplifying effect at –55 mV occurs due to
167 prominence of the amplifying NaP current in that voltage range, whereas the resonance
168 visible at –70 mV is due to the HCN current that dominates that voltage range. This
169 conclusion was supported by the fact that application of 1 μM TTX ($n = 9$ neurons, $N = 4$
170 mice), that abolished autonomous spiking and slightly hyperpolarized the CIN (Fig. 2A),
171 reduced the impedance ($P = 9 \cdot 10^{-9}$) and exhibited a trend toward a shortened phase delay (P
172 $= 0.137$, ANCOVA, Fig. 2B). These changes are captured by the amplification parameter
173 being estimated as less negative ($\mu_n = -2.0$), which reduces ϕ_s (Eq. 4, in Materials and

174 Methods). Similarly, application of 10 µM ZD7288, the selective HCN antagonist ($n = 9$
175 neurons, $N = 7$ mice), which abolished the sag response (Fig. 2C), abolished the resonance
176 peak in the impedance curve ($P = 4{\cdot}10^{-16}$) and significantly reduced the negative lobe in the
177 phase delay ($P = 0.018$, ANCOVA, Fig. 2D), which was captured by the resonance
178 parameter being reduced to $\mu_h = 0.5$.

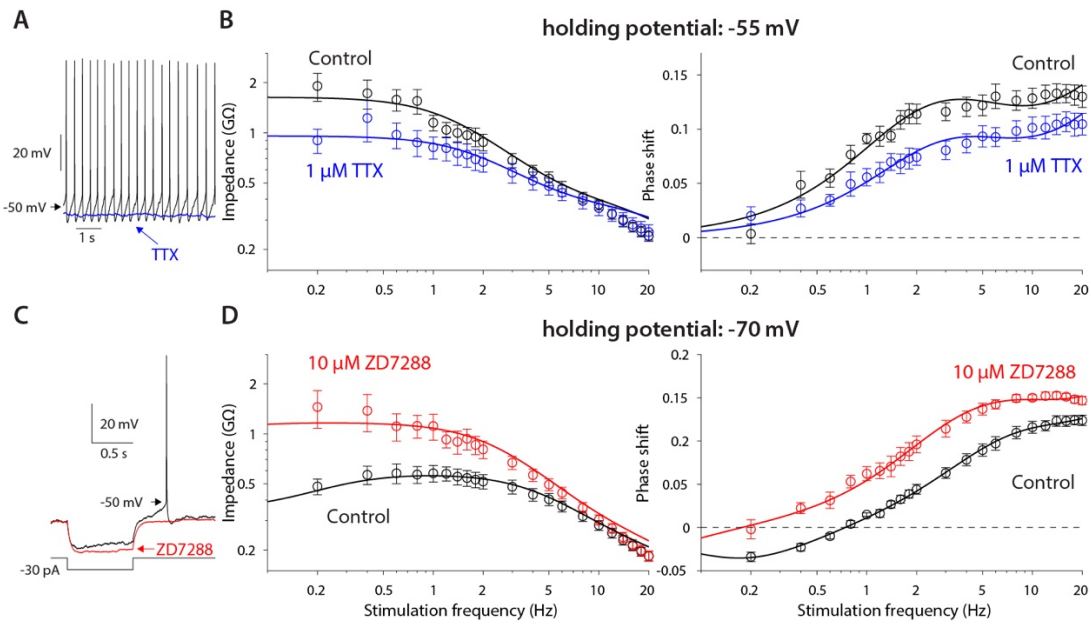

Figure 2: Amplification is caused by NaP currents, whereas the resonance is caused by HCN currents. A. TTX (blue) prevents autonomous spiking (black). **B.** TTX prevents amplification of the impedance (left), and reduces the phase shift (right). **C.** ZD7288 (red) abolishes the voltage sag (black). **D.** ZD7288 abolishes the resonance peak in the impedance, and the negative phase shifts in the subhertz range. Solid lines are parameter fits as in Fig. 1.

179 <u>Optogenetic interrogation of the spatial distribution of NaP and HCN currents in the CIN</u>
180 <u>dendritic arbor</u>

181 While the above experiments demonstrate the NaP and HCN currents are capable of
182 transforming subthreshold voltage fluctuations, the question remains as to where within the
183 CIN's somatodendritic compartments these currents perform their amplifying and restorative
184 actions, respectively. One extreme scenario is that they are restricted to the axosomatic region
185 (where they are needed for sustaining the autonomous firing patterns of the CINs). In that
186 scenario, the dendrites could be entirely linear, passively transmitting the distal
187 depolarizations to the soma. Only at the soma are the inputs then transformed by these
188 currents. However, a more realistic scenario is that these currents are also expressed
189 dendritically and exert their nonlinear influence on synaptic inputs more distally. But in this
190 scenario, we would still want to know where along the dendrites the currents are expressed.

191 To determine the precise location of these channels would require advanced *in situ* molecular
192 and anatomical techniques and/or direct electrophysiological recordings from CIN dendrites
193 in conjunction with advanced imaging techniques. While these experiments may, in principle,
194 be done, we wondered whether the optogenetics-based technique that we recently developed
195 to interrogate the role of dendrites in synaptic integration (Tiroshi and Goldberg, 2019) could
196 help us address this question.

197 We previously showed that the impact of dendrites on synaptic integration can be
198 quantified by studying the response of neurons that express ChR2 post-synaptically to (470
199 nm) illumination of their dendritic arbor. In particular, we compared between two spatial
200 patterns of illumination of the somatodendritc arbor of SNr neurons: either a small
201 perisomatic region (approximately 100 μm in diameter) or the entire dendritic arbor. By
202 using sinusoidally-modulated blue LED illumination at various temporal frequencies, we
203 were able to calculate the phase delays produced by both spatial patterns, and found that
204 illumination of the entire dendritic arbor introduced larger phase delays. In order to quantify
205 the effect, we fit the data to a tractable theoretical model of a semi-infinite cable (Goldberg et
206 al., 2007; Tiroshi and Goldberg, 2019). As mentioned above, in the case of the SNr neuron,
207 we found that the dendrites were well-fit by a passive linear cable model, whose parameters
208 (i.e., time and space constants) we could estimate. The conclusion that SNr dendrites were
209 largely linear was further supported by the finding that these phase delays were voltage-
210 independent (Tiroshi and Goldberg, 2019).

211 Because CINs exhibit prominent amplifying and resonating currents that are strongly
212 voltage dependent (Figs. 1 & 2), we posited that by using the same optogenetic technique and
213 semi-infinite cable model we would be able to quantify the contribution of CIN dendrites to
214 post-synaptic integration. In particular, we hypothesized that by fitting a *quasi-linear* cable
215 model we would be able to quantify to what degree CIN dendrites *per se* possess amplifying
216 or resonating properties (See Materials and Methods). Finally, by comparing illumination of
217 the proximal *vs.* the entire dendritic arbor, we could learn something about the localization of
218 the nonlinearities along the dendritic arbor. To this end, we crossed mice that express Cre-
219 recombinase under a ChAT promoter with the Ai32 mouse that expresses ChR2 and EYFP in
220 a Cre-dependent manner (see Materials and Methods). The cholinergic neuropil and
221 individual CINs could be clearly visualized in the dorsal striatum of these ChAT-ChR2 mice
222 (Fig. 3A). Individual CINs were patched and recorded in voltage clamp, while illuminating

either the proximal region with a 60X water-immersion objective (Fig. 3A) or the entire slice with a 5X air objective, with a continuous sequence of sinusoidally modulated illumination waveforms at various frequencies (Fig. 3B, blue).

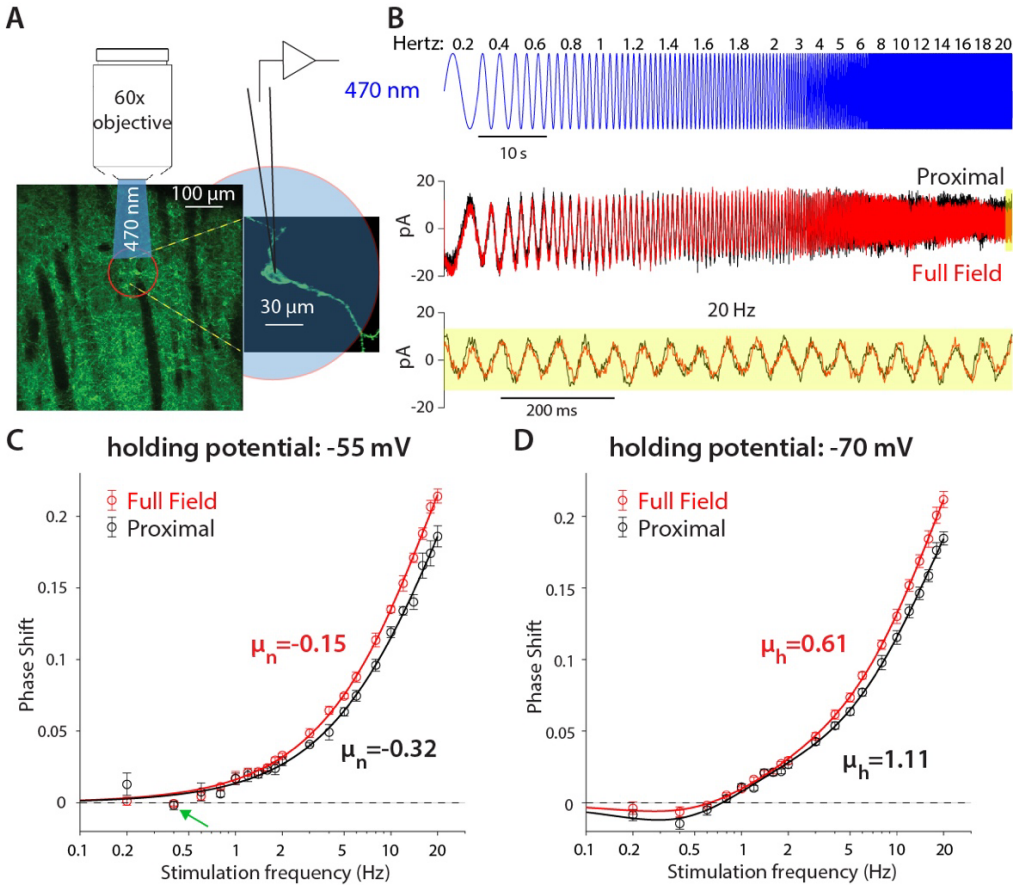

Figure 3: Optogenetic interrogation of the quasilinear properties of CIN dendrites indicates that dendritic nonlinearities are more prominent proximally. A. A CIN in a sagittal slice from ChAT-ChR2 mouse is patch-clamped in the whole-cell mode while either a small proximal region around the soma or the full-field are illuminated with a sinusoidally modulated 470 nm LED. **B.** The current response to the proximal (black) and full-field (red) illumination differ, with the phase of the full-field illumination right-shifted at the higher frequencies (20 Hz is highlighted in yellow). **C.** Phase shifts at –55 mV holding potential, calculated for proximal (black) and full-field illumination (red). A tendency towards negative phase shifts is present at 0.4 Hz (green arrow). **D.** Phase shifts at –70 mV holding potential, exhibit a negative phase shift. Fitting the quasi-linear model at –55 mV demonstrate the magnitude of the amplification parameter (μ_n) is smaller for the full field fit (Eqs. 1-3). Similarly, at –70 mV the resonance parameter (μ_h) is smaller for the full field fit. The elevation in these parameters' magnitudes when illuminating proximally relative to full-field suggest that the surface densities of NaP and HCN currents is higher proximally.

Comparison of the somatic current traces in response to proximal (Fig. 3B, black) vs. full-field (red) illumination demonstrated that the phase of the full-field-generated current is delayed relative to the proximally-generated current. This could be observed in the raw data both for the low and high (yellow inset) frequencies. The effect at the high frequency was very evident when plotting the phase delay curves both when the CINs were held at –55 mV

(Fig. 3C) and at –70 mV (Fig. 3D). Estimation of the phase delays revealed delays that were considerably larger than those observed with the electrical somatic stimulation (Fig. 1). Thus, to account for these large delays (Figs. 3C&D), we fit a model of the sum of a somatic delay, ϕ_s (Eq. 4, in Materials and Methods), and a dendritic delay, ϕ_d (Eq. 1, in Materials and Methods). For the curve calculated at the –55 mV holding potential ($n = 5$ neurons, $N = 4$ mice), we fit a model with only an amplifying current. As expected, the fits were significantly different ($P = 4 \cdot 10^{-3}$, ANCOVA) and extracted a larger effective radius (in units of space constants) of $r = 1.47$ for the full field stimulation as compared to $r = 0.79$ (See Materials and Methods). Additionally, the amplifying parameter was more negative ($\mu_n = -0.32$) for the proximal fit than for the full field fit ($\mu_n = -0.15$). At face value, this latter finding means that the amplifying nonlinearity appears denser when activating only the proximal arbor, than when activating the entire arbor. In other words, this finding suggests that the NaP currents are denser more proximally and probably drop off farther out in the CIN dendrites.

A closer look at the fits (at the –55 mV holding potential) reveals that the phase delay at 0.4 Hz (for both the proximal and full field illumination), is not captured by this model. This dip in phase delay (Fig. 3C, green arrow) at this low frequency is reminiscent of what a restorative current is expected to do. In order to accentuate the effect of the restorative HCN currents, we repeated the experiment at the –70 mV holding potential (Fig. 3D). In this case ($n = 14$ neurons, $N = 10$ mice), the phase delays at the lower frequencies (especially at 0.4 Hz) were negative, which was reminiscent of the results from the electrical voltage stimulation experiments (Fig. 1) at the –70 mV holding potential.

When fitting a full soma-plus-dendrite model (incorporating both amplifying and restorative parameters) the fits were significantly different ($P = 8 \cdot 10^{-4}$, ANCOVA) and the differences between the estimates of the effective radii were larger: $r = 1.4$ for the full-field *vs.* $r = 0.41$ for the proximal illumination. Here too the restorative parameter was estimated to be larger for the proximal fit ($\mu_h = 1.11$) relative to the full field fit ($\mu_h = 0.61$), suggesting that the HCN currents are denser more proximally. This conclusion is buttressed by the fact that the negative phase delays in the subhertz frequency range tended to be less negative for the full-field illumination ($P = 0.037$, Wilcoxon rank sum test on phase delays at 0.4 Hz). In the framework of our quasi-linear model, the only mathematically possible way to recreate this finding while increasing the effective radius r is by reducing the restorative parameter μ_h.

Otherwise, if μ_h were constant then illuminating a larger region of the cable – by increasing r – would necessarily recruit more restorative current, thereby making the negative delays more negative. Thus, the conclusion of our analysis is that CIN dendrites indeed express the amplifying and resonating nonlinearities, which can contribute to post-synaptic integration. Moreover, the analysis strongly suggests that these nonlinearities are concentrated proximally and likely taper off distally. In the following section, we provide independent evidence in support of this conclusion vis-à-vis NaP currents.

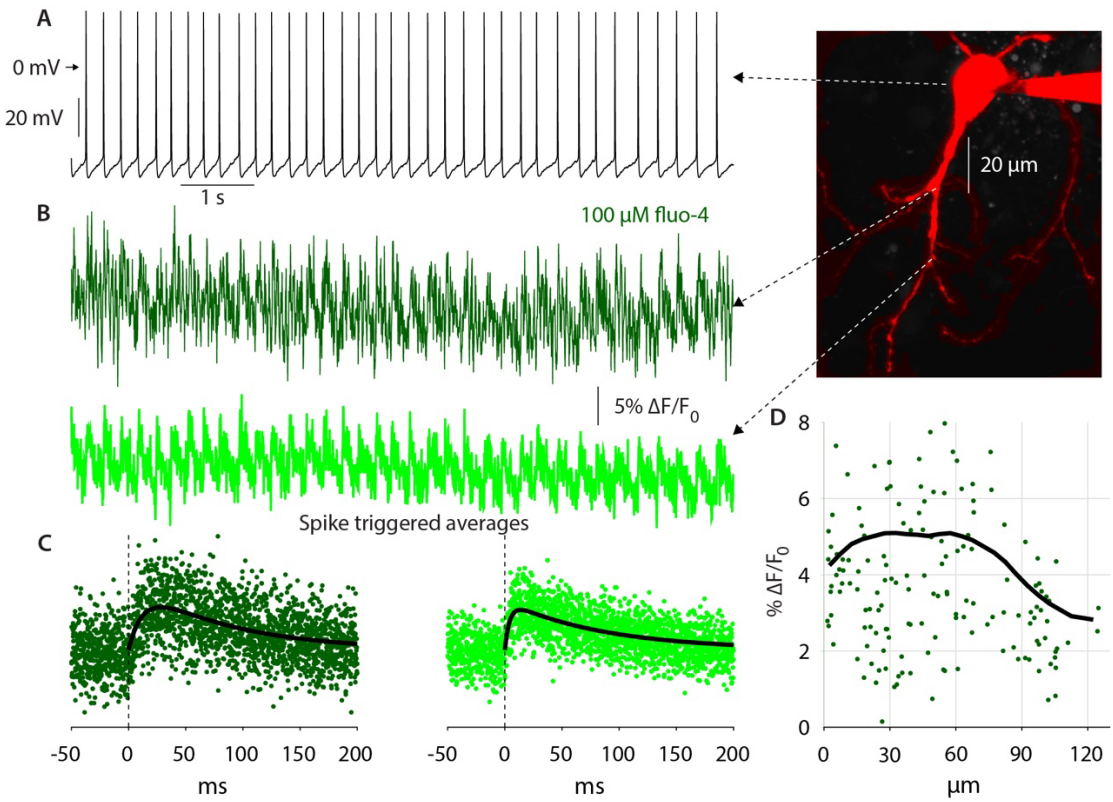

Figure 4: Autonomous action potentials actively back-propagate in CIN dendrites up to 70 µm from the soma. A. Autonomous discharge of a CIN that was patched and filled with fluo-4 and Alexa Fluor 568 for 2PLSM imaging (image). **B.** Line scans at various distances from the soma exhibit Ca^{2+} oscillations caused by bAPs. **C.** Calculating the spike-triggered average of these oscillations and fitting an alpha-function gives an estimate of the amplitude of these oscillations (in % $\Delta F/F_o$). **D.** The scatter plot of these amplitudes as a function of distance from the soma (11 CINs from 7 mice are pooled) exhibits a large degree of variability. However, a 35 µm moving average (black line) exhibits that the Ca^{2+} transients begin to decay approximately 70 µm from the soma, indicating that bAPs are supported by Nav channels up to that point (the initial increase up to 20 µm is due to the increase in the surface-to-volume ratio in the large proximal dendrites).

<u>Distance of dendritic bAP invasion indicates location of amplifying Nav channels</u>

The persistent and fast-inactivating Nav currents flow through the same Nav channels (Alzheimer et al., 1993). Therefore, determining to what distance from the soma dendritic bAPs invade provides a measure of the Nav channels density – and therefore where the NaP

274 current is present – in the dendritic arbor. To this end, we used 2PLSM Ca^{2+} imaging to
275 measure the size of the Ca^{2+} transients elicited by bAPs in autonomously firing CINs at
276 various distances from the soma (Fig. 4A). We conducted line scans (*n = 11* neurons, *N = 7*
277 mice) to measure the Ca^{2+} signals at various distances from the soma (Fig. 4B). Next, we
278 estimated the size of the spike triggered average (STA) of the $\Delta F/F_0$ Ca^{2+} signal, by
279 averaging around spontaneous APs measured at the soma (Fig. 4C). The amplitude of the
280 STA was estimated by fitting it with an alpha-function (see Materials and Methods). A scatter
281 plot of STA amplitude *vs.* distance from soma demonstrates a large degree of variability (Fig.
282 4D). Nevertheless, applying a 35 µm moving average to the scatter plot reveals a trapezoidal
283 dependence of Ca^{2+} transient sizes (Fig. 4D, black). The initial dip in the size of the transients
284 at short distances from the soma result from the large size of the proximal dendrites (Fig.
285 4D), which reduces the size of the Ca^{2+} transient due to the low surface-to-volume ratio of the
286 thick proximal dendrites. Neglecting that effect, we found that the size of the bAP driven
287 Ca^{2+} transients remains constant up to approximately 70 µm from the soma, and then drops
288 off. This spatial dependence of the Ca^{2+} transient amplitude, suggests that the bAP maintains
289 a constant amplitude due to the presence of Nav channels that sustain their regenerative
290 nature out to some 70 µm from the soma. Farther out the Ca^{2+} transients decrease presumably
291 due to a drop off in Nav channel expression, which leads to a lower amplitude bAPs, and
292 hence less Ca^{2+} via voltage-activated Ca^{2+} channels. Thus, this measurement strengthens the
293 conclusion that NaP currents are present in CIN dendrites – primarily in proximal dendrites
294 (up to approximately 70 µm from the soma).

295 <u>NaP currents boost proximal thalamic inputs but not distal cortical inputs to CINs</u>

296 The above data indicate that Nav channels are preferentially expressed in proximal
297 dendrites. Therefore, their ability to boost small voltage perturbations, including synaptic
298 inputs, should be restricted to proximal dendrites. Because thalamic inputs terminate
299 proximally, whereas cortical inputs terminate distally (Doig et al., 2014; Lapper and Bolam,
300 1992; Thomas et al., 2000), we would expect only the former to be boosted by Nav current.
301 To test this, we transcranially inoculated the PfN of Vglut2-ires-Cre mice with adeno-
302 associated viruses (AAVs) harboring Cre-dependent ChR2 and EYFP genes (Fig. 5A)
303 (Aceves Buendia et al., 2019; Rehani et al., 2019). Two weeks later, we tested the sensitivity
304 of optogenetically-evoked EPSPs to ranolazine (30 µM), a selective antagonist of the NaP
305 current, in CINs patched in acute striatal slices. The mean amplitude of the EPSP was

306 reduced by a median of 16% (*n = 11* neurons, *N = 4* mice, *P = 0.04*, Wilcoxon signed-rank
307 test, Fig. 5B). In order to test whether the more distal cortical inputs are modulated by NaP,
308 we used the Thy1-ChR2 mice (Aceves Buendia et al., 2019; Arenkiel et al., 2007) that
309 expressed ChR2 in corticostriatal fibers (Fig. 5C). The EPSPs elicited by cortical inputs to
310 CINs in these mice were unaffected by ranolazine (*n = 11* neurons, *N = 6* mice, *P = 0.74*,
311 Wilcoxon signed-rank test, Fig. 5D). Thus, the post-synaptic modulation of glutamatergic
312 inputs to CINs by NaP currents corresponds to the spatial distribution of these currents as
313 derived from our analysis of the quasi-linear properties of CINs and 2PLSM imaging of
314 bAPs.

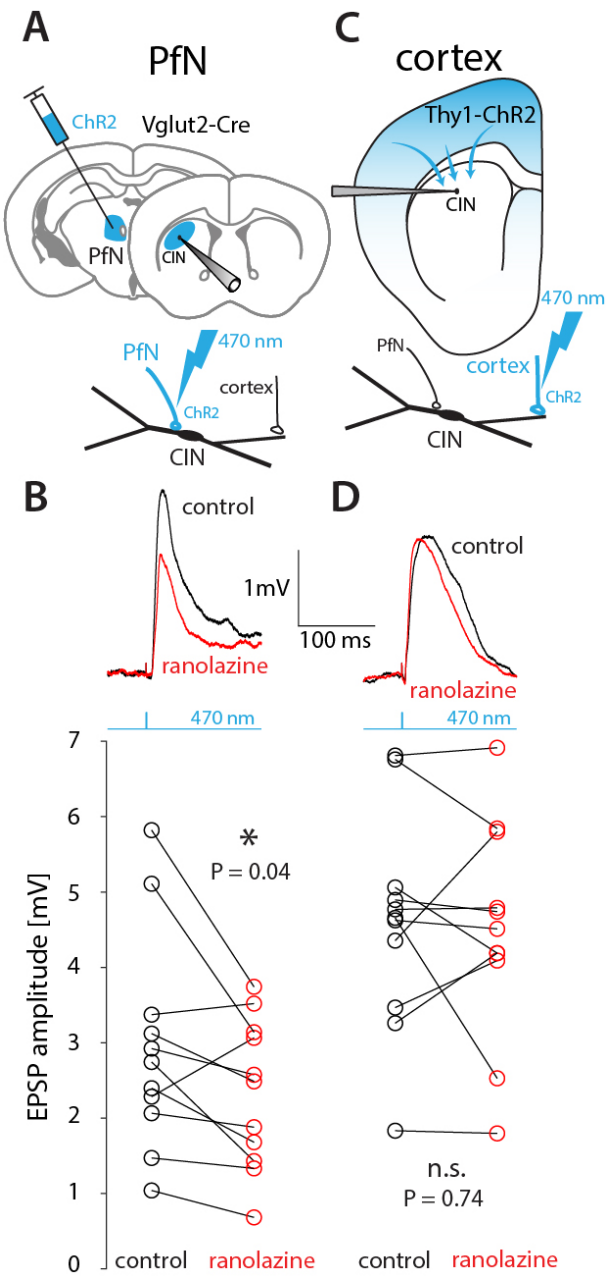

Figure 5: Thalamic – but not cortical EPSPs – onto CINs are boosted by NaP currents in healthy mice. A. The parafascicular nucleus (PfN) of Vglut2-Cre mice was inoculated with AAVs harboring Cre-dependent ChR2, so that 470 nm LED illumination of striatal slices activated PfN terminals while CINs were patched in current clamp mode. **B.** Optogenetically evoked thalamic EPSPs in CINs (held between –50 mV and –60 mV) were reduced by 30 µM ranolazine. **C.** CINs were patched in current clamp in Thy1-ChR2 mice, so that 470 nm LED illumination of striatal slices activated nominally cortical terminals. **D.** Optogenetically evoked cortical EPSPs were unaffected by ranolazine.

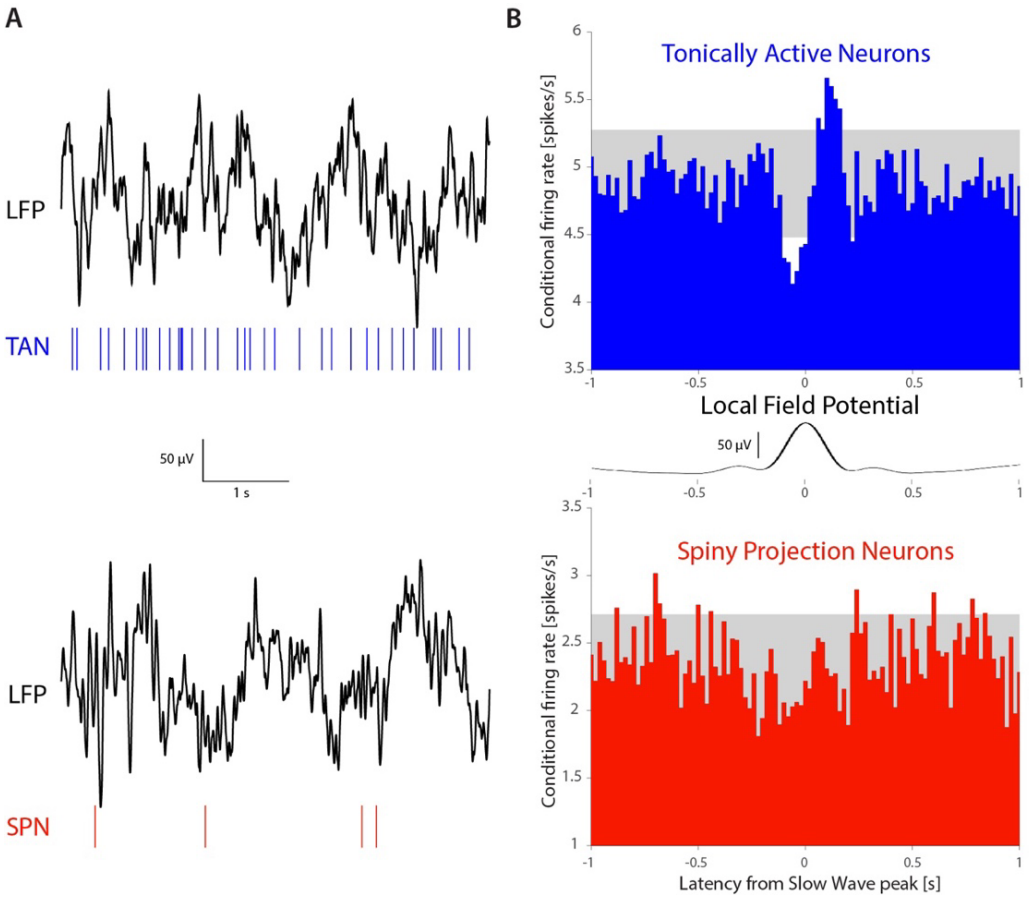

Figure 6: TANs, but not SPNs, exhibit a pause-like response to slow-wave events occurring during natural non-REM sleep in non-human primates (NHPs). A. Top: simultaneous recording of LFP and a TAN in an NHP during N2 and N3 stages of sleep. Bottom: simultaneous recording of LFP and an SPN in an NHP during N2 and N3 stages of sleep. **B.** Top: TAN firing rate conditioned on the occurrence of an LFP slow wave event (28,603 triggers). Middle: Average striatal LFP signal triggered on the occurrence of slow wave events (see Materials and Methods). Bottom: SPNs firing rate conditioned on the occurrence of slow wave event (6,065 triggers). Gray box indicates the 99% confidence intervals.

<u>Tonically active neurons in non-human primates exhibit a pause-like response to slow wave oscillations during sleep</u>

Our data, alongside previous studies (Beatty et al., 2015), demonstrate that somatodendritic HCN currents give rise to resonances in the subhertz range in CIN surface membranes. In contrast, SPNs exhibit no resonance (Beatty et al., 2015). This suggests CINs in intact animals may exhibit increased sensitivity to oscillatory inputs in that frequency range, whereas SPNs should not. Delta waves in the electroencephalogram (EEG) and in cortical and sub-cortical local field potentials (LFP) are prominent during non-REM sleep across species (Brown et al., 2012; Liu and Dan, 2019), including in non-human primates (NHPs) (Mizrahi-Kliger et al., 2018). Because the LFP is widely thought to represent

326 subthreshold cellular activity, affected by afferent and recurrent synaptic inputs (Buzsáki et
327 al., 2012), we hypothesized that the tonically active neurons (TANs) in the NHP striatum –
328 that are comprised primarily of CINs (Aosaki et al., 1995; Kawaguchi, 1993; Wilson et al.,
329 1990) – will exhibit stronger entrainment to slow-wave LFP events during sleep, while SPNs
330 under the same conditions will not. Indeed, triggering the spike trains of TANs and SPNs
331 (from $N = 2$ NHPs) on slow wave events that occur during sleep stages N2 and N3 (Mizrahi-
332 Kliger et al., 2018; Riedner et al., 2007), which represent relatively deep non-REM sleep,
333 demonstrates that the firing rates of TANs ($n = 122$) is modulated by these slow-wave events,
334 whereas the firing rate of SPNs ($n = 83$) is not. Importantly, the biphasic response exhibited
335 by TANs to slow-wave events bears a striking resemblance to the "classical" TAN response
336 to external cues (Aosaki et al., 1995; Apicella et al., 1991; Joshua et al., 2008; Kimura et al.,
337 1984). Because these responses in awake primates require an intact thalamic projection
338 (Bradfield et al., 2013; Goldberg and Reynolds, 2011; Matsumoto et al., 2001; Schulz and
339 Reynolds, 2013; Smith et al., 2004; Yamanaka et al., 2018) (and there is no reason to assume
340 that this is altered in sleep), they provide support to the hypothesis that the CIN membrane
341 resonance contributes to a thalamically-driven biphasic CIN response during slow-wave
342 sleep. Importantly, because the primates are asleep in a sound-proof room, this is, to the best
343 of our knowledge, the first report of striatal TANs responding to an internally-generated brain
344 event, and not an external saliency-related cue.

345 Discussion

346 Quasi-linear dendritic properties of CINs and the non-uniform distribution of their active
347 conductances

348 In the current study, we applied a cable-theoretic and optogenetics-based formalism –
349 that we developed previously to study dendritic properties of SNr neurons (Tiroshi and
350 Goldberg, 2019) – to study the dendritic properties of CINs. Unlike SNr neurons that were
351 found to act like passive linear cables exhibiting no voltage dependent properties, we find
352 that CIN dendrites exhibit both amplification and resonances in a voltage dependent manner:
353 amplification is more prominent at depolarized subthreshold potentials (approximately –55
354 mV), whereas resonances are more prominent at more hyperpolarized potentials
355 (approximately –70 mV). Moreover, we found that our method is able to provide information
356 about where in the dendritic arbor these quasi-linear properties are localized. We extracted
357 boosting (μ_n) and resonance (μ_h) parameters for proximal vs. full-field illumination, and

358 found that the magnitude of both parameters is smaller when the entire dendritic arbor is
359 illuminated. In other words, activating more of the distal dendritic membrane dilutes the
360 amplifying and resonating effects, meaning that the additional membrane illuminated in the
361 full-field condition contributed less to amplification and resonances. The simplest
362 interpretation of this finding is that the active conductances that give rise to amplification and
363 resonance are more highly expressed proximally and apparently taper off farther out in the
364 dendritic arbor. We identified the relevant currents by studying the quasi-linear properties of
365 CIN somata with voltage perturbations. We found that amplification is TTX sensitive and
366 therefore arises from Nav channels, that give rise to the NaP current. Similarly, we found that
367 resonances require HCN channels.
368 We used two indirect methods to validate the preferentially proximal localization of
369 NaP currents. First, we implemented a widely-used approach of estimating the distance of
370 dendritic invasion of bAPs by imaging the Ca^{2+} influx that accompanies them (Carter and
371 Sabatini, 2004; Day et al., 2008; Goldberg et al., 2009; Kerr, 2004; Rehani et al., 2019;
372 Tanimura et al., 2016). We found – not unlike in SPN neurons – that bAPs maintain their
373 amplitude out to 70 µm from the soma and then begin to decay, suggesting that Nav currents
374 that support bAP propagation taper off from that point onwards. Future work can verify this
375 by directly testing where locally puffed TTX attenuates the bAP (perhaps even with the use
376 of voltage sensitive probes). Second, we demonstrated that only thalamic – but not cortical –
377 EPSPs exhibit sensitivity to the selective NaP blocker. Because the thalamic terminals are
378 located more proximally (Lapper and Bolam, 1992; Thomas et al., 2000), this provides
379 further evidence that NaP currents are more prominent locally. The preferential localization
380 of HCN currents proximally in CIN dendrites requires additional validation, particularly
381 because other neurons exhibit an opposite pattern (Berger et al., 2001). However, we were
382 less interested in validating the proximal localization of HCN currents, because unlike NaP
383 currents, activation of HCNs is conditioned on CINs being actively (after-)hyperpolarized,
384 during which bAPs are unlikely to occur. We did however test a context in which HCN
385 currents, and the resonance they underlie, are likely to affect CIN collective dynamics. We
386 found that TANs respond biphasically to internally-generated slow wave activity during
387 sleep. This preferential entrainment is consistent with the fact that CIN membranes exhibit a
388 resonance in the subhertz range as found by us and others (Beatty et al., 2015). The elevated
389 impedance (or frequency dependent access resistance) in this range means that inputs
390 fluctuating in this range will more efficiently depolarize the CINs and therefore more likely
391 to trigger additional action potentials than inputs fluctuating at a frequency that is far from

392 the resonance frequency. Accordingly, SPNs that do not exhibit resonances (Beatty et al.,
393 2015) are not entrained by the slow wave oscillation. Our findings in sleeping NHPs are at
394 odds with a rodent study by Sharott and collaborators (Sharott et al., 2012) that found only a
395 weak association between cortical slow-wave activity and the discharge of TANs in
396 anesthetized mice. Moreover, they reported a stronger association of SPNs with the slow
397 wave activity. These differences may be attributable to species differences and/or differences
398 between natural sleep and anesthesia.

399 Advantages and limitations of the quasi-linear formalism and the optogenetics-based
400 approach

401 As mentioned in the introduction, the quasi-linear approach provides a tool to
402 characterize membrane excitability in general functional terms, without requiring the
403 complete biophysical characterization of membrane currents. Unfortunately, the method is
404 not invertible: even after estimating all the quasilinear parameters one cannot deduce the full
405 biophysical characterization of the underlying channels even if one has a precise
406 mathematical model of these channels. Moreover, even though we extracted the values of μ_n
407 and μ_h, we do not know how to translate them into a quantitative measure of channel density,
408 or have a proper explanation as to why the somatic values of these parameters (estimated
409 with voltage perturbations) are larger than the dendritic ones. Still, the ability to compare
410 parameters for various spatial illumination patterns enables us to reach qualitative
411 conclusions regarding relative channel density. Additionally, our attribution of μ_n to NaP and
412 μ_h to HCN is only provisional. CINs possess other channels that have a major influence on
413 their firing patterns such as A-type, inward rectifying, and various Ca^{2+}-activated K^+
414 channels, to mention a few (Bennett et al., 2000; Deng et al., 2007; Goldberg et al., 2009;
415 Goldberg and Wilson, 2010, 2005; McGuirt et al., 2021; Oswald et al., 2009; Song and
416 Surmeier, 1996; Wilson, 2005; Wilson and Goldberg, 2006), that were not included in our
417 analysis. Future work, should elaborate how these and other channels contribute to the quasi-
418 linear properties of CINs and their dendrites.
419 Using optogenetics provides another level of practicality. The seminal studies that
420 characterized the filtering properties of dendrites or pyramidal neurons (Berger et al., 2001;
421 Goldberg et al., 2007; Hutcheon et al., 1996; Ulrich, 2002) required dual soma-dendrite
422 patching which is not practical for all neuronal types whose dendrites taper off rapidly.
423 Expressing opsins in the membrane being activated, as we did, means that a single somatic

424 patch electrode can suffice to conduct the quasi-linear characterization. We currently use this
425 approach to illuminate large regions of the dendritic arbor simultaneously, which means we
426 can only derive large-scale dendritic properties. In the future, localized laser stimulation of
427 dendritic regions (visualized with the help of a fluorescent marked in the patch pipette), or
428 even two-photon laser activation of opsin (provided one can find stimulation parameters that
429 do not harm the dendrites) could be used as an alternative approach. Another point to
430 consider is that the temporal kinetics of the opsin also introduces additional linear filtering of
431 the input (Higgs and Wilson, 2017; Tiroshi and Goldberg, 2019). However, by demonstrating
432 differential responses to various spatial patterns we circumvent this concern. On the backdrop
433 of optogenetics being utilized almost exclusively to study circuit mapping (Häusser, 2021;
434 Kim et al., 2017) by expressing opsins presynaptically, we believe our study joins other
435 studies (Higgs and Wilson, 2017; Tiroshi and Goldberg, 2019) to underscore the value of
436 using opsins expressed postsynaptically to study neuronal – even dendritic – excitability.

437 Somatic amplification and resonance in CINs

438 We preceded our optogenetic characterization of dendritic nonlinearities with the
439 electrical characterization of quasilinear somatic properties using a sinusoidal voltage
440 command applied through the patch pipette. As previously reported by Beatty and
441 collaborators (Beatty et al., 2015), CIN somata exhibit a membrane resonance in the subhertz
442 range, that depends on the holding potential. However, while Beatty and collaborators found
443 that an amplified resonance is present in the more depolarized (approximately – 55 mV)
444 range, we found that the resonance is only pronounced in the more hyperpolarized
445 (approximately –70 mV) range, where it depends on the HCN current. It is possible that the
446 resonances observed by Beatty and collaborators (2015) at –55 mV arose from ineffective
447 clamping of dendrites with the slightly higher resistance electrodes used in that study. In
448 support of this proposition, we also found evidence for the resonance arising from unclamped
449 (dendritic) membranes. When the CINs were clamped at –55 mV, while somatic voltage
450 perturbations did not produce a resonance, optogenetic stimulation (both proximal and full
451 field) at 0.4 Hz produced a more negative phase than at the neighboring 0.2 Hz and 0.6 Hz
452 stimulation (Fig. 3C, green arrow). This downward deflection in phase is reminiscent of the
453 full flown negative subhertz region that occurred with optogenetic stimulation when the CINs
454 were clamped at –70 mV. Thus, it is likely that resonance originated in both studies from
455 dendritic HCN currents. Because in the study of Beatty and collaborators (Beatty et al., 2015)

456 TTX lowered the impedance, without removing the subhertz resonance peak, we conclude
457 that the effect of TTX in both studies is to remove the NaP-dependent boosting, without
458 directly affecting resonance.

459 Dendritic contribution to capacity of CINs to differentiate between their excitatory inputs

460 In NHPs, TANs that are comprised primarily of CINs (Aosaki et al., 1995; Goldberg
461 and Wilson, 2010; Kawaguchi, 1993; Wilson et al., 1990), encode – through a brief pause in
462 their tonic firing – external stimuli that are salient (and often unexpected, even conveying a
463 stop or behavioral shift signal (Aoki et al., 2018; Thorn and Graybiel, 2010)) or stimuli that
464 are associated with reward (Apicella et al., 1991; Goldberg and Reynolds, 2011; Kimura et
465 al., 1984). The pause response requires an intact projection from the parafascicular nucleus
466 (PfN) of the thalamus (Bradfield et al., 2013; Goldberg and Reynolds, 2011; Matsumoto et
467 al., 2001; Schulz et al., 2011; Schulz and Reynolds, 2013; Smith et al., 2004; Yamanaka et
468 al., 2018), indicating that TANs are attuned to thalamic input. While TANs do not respond to
469 ongoing movement (Aosaki et al., 1994; Apicella et al., 1991; Kimura et al., 1984; Raz et al.,
470 1996), and hence seem less attuned to sensorimotor cortical input (Sharott et al., 2012), CIN
471 activity in awake behaving mice is strongly modulated by self-initiated movements (Gritton
472 et al., 2019; Howe et al., 2019; Yarom and Cohen, 2011). Nevertheless, slice physiology
473 studies in rodents (Aceves Buendia et al., 2019; Assous, 2021; Assous et al., 2017; Ding et
474 al., 2010; Johansson and Silberberg, 2020; Kosillo et al., 2016; Threlfell et al., 2012) clearly
475 show that thalamic inputs to CINs are stronger in the sense that they give rise to larger EPSPs
476 (Johansson and Silberberg, 2020) and can trigger a pause-like responses (Ding et al., 2010),
477 whereas cortical inputs to CINs are weaker in that they give rise, in acute slices, to smaller
478 EPSPs and cannot trigger the pause-like response – although this distinction is less
479 pronounced in anesthetized rodets (Doig et al., 2014). Thus, it is clear that CINs differentiate
480 between these two excitatory inputs and respond differently to them. A major contributor to
481 the CINs' capacity to dissociate thalamic and cortical input is the differential distribution of
482 their respective terminals on the dendritic arbor: thalamic input terminate perisomatically and
483 on proximal dendrites, whereas cortical input terminates on distal dendrites (Doig et al.,
484 2014; Lapper and Bolam, 1992; Thomas et al., 2000). Our finding that the higher expression
485 of NaP currents in proximal dendrites preferentially boosts thalamic over cortical inputs,
486 suggests that active conductances are expressed in CIN dendrites in a manner that

487 corresponds and reinforces the effect of the spatial separation between the terminals of the
488 two inputs.

489 Adaptive changes in dendritic excitability in movement disorders

490 The capacity of the CIN dendritic excitability to mirror the distribution of afferent
491 terminals is also an adaptive process. We previously reported that CIN dendritic excitability
492 is elevated in the Q175 mouse model of Huntington's disease (HD) (Tanimura et al., 2016).
493 In contrast to control (Thy1-ChR2) mice in which cortical EPSPs in CINs are insensitive to
494 ranolazine (Fig. 5), cortical excitatory postsynaptic currents (EPSCs) in CINs from Q175
495 mice (crossed with Thy1-ChR2 mice) are strongly reduced by ranolazine. The acquired
496 dependence of distal cortical inputs on NaP currents in Q175 mice results from an
497 upregulation of the NaP current, which was also evidenced by bAPs invading farther out into
498 the CINs' dendritic arbor (Tanimura et al., 2016). This elevated excitability in the Q175
499 mouse is probably a homeostatic response aimed at elevating the postsynaptic sensitivity to
500 the remaining synaptic contents after the loss of afferent cortical and thalamic inputs
501 observed in HD mouse models (Deng et al., 2013). Because thalamostriatal inputs are also
502 altered in models of Parkinson's disease (PD) (Aceves Buendia et al., 2019; Parker et al.,
503 2016; Tanimura et al., 2019), future work should determine whether the excitability of CIN
504 dendrites is altered in these models, as well. Importantly, dendrites are positioned at the
505 interface between synaptic inputs and the intrinsic properties of CIN. While changes in
506 synaptic transmission and intrinsic excitability of CINs have received attention in models of
507 PD, HD and other movement disorders (Abudukeyoumu et al., 2019; Aceves Buendia et al.,
508 2019; Choi et al., 2020; Ding et al., 2006, 2011; Eskow Jaunarajs et al., 2015; Mallet et al.,
509 2019; Paz et al., 2021; Pisani et al., 2007; Plotkin and Goldberg, 2019; Poppi et al., 2021;
510 Tanimura et al., 2019; Tubert and Murer, 2021), studying alterations in dendritic excitability
511 in these models is a complementary approach that remains a largely unchartered territory.
512 The membrane channels that are expressed in CINs (e.g., Nav, HCN, Kv4, etc.) are
513 targets for neuromodulation under normal, healthy circumstances (Deng et al., 2007; Helseth
514 et al., 2021; Maurice, 2004; Song and Surmeier, 1996). Therefore, it is likely that the
515 dendritic excitability of CINs can be modulated under physiological conditions, as well, as a
516 way to adjust the tuning of CINs to their afferent inputs. Conversely, if boosting and
517 resonances are present primarily proximally, the selective tuning of CINs to subhertz slow-
518 wave oscillations is probably stronger for thalamic inputs (that terminate proximally) than for

519 cortical inputs. Future experiments can address this issue by testing how silencing the PfN
520 affects the observed entrainment of TANs to slow-waves (Fig. 6).
521 In summary, we have used a new optogenetics-based approach, complemented by
522 other electrophysiological and imaging approaches, to demonstrate that the spatial
523 localization of active dendritic conductances that endow CIN dendrites with quasi-linear
524 filtering properties corresponds to the spatial distribution of their two main afferent excitatory
525 inputs. This matching up of presynaptic terminals with post-synaptic excitability, probably
526 contributes to the capacity of CINs to respond differentially to cortical and thalamic inputs.
527 Sensorimotor information of cortical origin seems to be integrated continuously in a moment-
528 by-moment fashion. In contrast, thalamic inputs lead to abrupt pauses in TAN firing, even in
529 response to internally-generated brain-states (e.g., during slow-wave activity). The fact that
530 dendritic arbors adapt to the spatiotemporal patterns of afferent inputs is likely an important
531 principle of neural computation that deserves further attention, particularly in the framework
532 of autonomously active neurons such at CINs, SNr neurons and other basal ganglia
533 pacemakers.
534

535 ## Materials and Methods

536 Ethics statement: All experimental protocols were conducted in accordance with the National
537 Institutes of Health Guide for the Care and Use of Laboratory Animals, and with the Hebrew
538 University guidelines for the use and care of laboratory animals in research. The experiments
539 adhered to, received prior written approval and were supervised by the Institutional Animal
540 Care and Use Committee of the Faculty of Medicine.

541 Mice: Homozygous Ai32 (RCL-ChR2(H134R)/EYFP) mice (The Jackson laboratory [Jax]
542 stock: 012569) that express floxed ChR2 and an EYFP fusion protein under the CAG
543 promoter were crossed with homozygous ChAT-IRES-Cre (Δneo) mice the express Cre
544 recombinase under the choline acetyltransferase promoter (Jax stock: 031661). The ChAT-
545 ChR2 offspring (4-8 weeks old/both sexes) were used for the majority of experiments. To
546 investigate corticostriatal transmission, we used homozygous transgenic Thy1-ChR2 mice
547 (B6.Cg-Tg (Thy1-COP4/EYFP) 18Gfng/1, Jax stock: 007612), that express ChR2 under the
548 Thy1 promoter in cortical neurons (Arenkiel et al., 2007). To investigate thalamostriatal
549 transmission, we used Vglut2-ires-Cre mice (Jax stock: 016963).

550 Non-Human Primates (NHPs): Data were obtained from two healthy, young adult, female
551 vervet monkeys. The monkeys were habituated to sleeping in a primate chair, positioned in a
552 dark, double-walled sound-attenuating room. The primate chair restrained the monkeys' hand
553 and body movements but otherwise allowed them to be in a position similar to their natural
554 (sitting) sleeping posture. Detailed sleep habituation, surgery and sleep staging were reported
555 previously (Mizrahi-Kliger et al., 2018). For extracellular recordings, the monkeys' heads
556 were immobilized with a head holder and eight glass-coated tungsten microelectrodes were
557 advanced the dorsal striatum. Electrical signals were amplified with a gain of 20, filtered
558 using a 0.075 Hz (2 pole) to 10 kHz (3 pole) Butterworth filter and sampled at 44 kHz by a
559 16-bit analog/digital converter. Spiking activity was sorted online using a template matching
560 algorithm. The striatum was identified based on its stereotaxic coordinates according to MRI
561 imaging and primate atlas data (Martin and Bowden, 2000). Tonically active neurons (TANs)
562 and spiny projection neurons (SPNs) were identified using real-time assessment of their
563 electrophysiological features. Spiking and local field potentials (LFP) were recorded only for
564 identified recording sites with stable recording quality (i.e., where single-neuron spiking
565 yielded an average isolation score ≥0.85).
566 We followed established procedures for slow wave detection in the LFP (Riedner et al.,
567 2007). Briefly, the LFP signal was filtered at the 0.5-4 Hz range and putative slow wave events
568 whose duration was 0.25-2 seconds were kept for further analysis. Next, the slow wave peaks
569 were sorted according to their amplitude. Artifacts were removed by discarding all events
570 whose amplitude exceeded 5 standard deviations above the mean. Finally, conditional firing
571 rate analysis was only performed on 30% of the slow wave events with the highest amplitude.

572 Stereotaxic viral inoculation in Vglut2-ires-Cre mice: Mice were deeply anesthetized with
573 isoflurane in a non-rebreathing system (2.5% induction, 1-1.5% maintenance) and placed in a
574 stereotaxic frame (Kopf Instruments, Tujunga, CA). Temperature was maintained at 35˚C
575 with a heating pad, artificial tears were applied to prevent corneal drying, and animals were
576 hydrated with a bolus of injectable saline (10 ml/kg) mixed with analgesic (2.5 mg/kg
577 Meloxicam). Stereotaxic injections into caudal intralaminar nuclei of thalamus were
578 performed under aseptic conditions. Adeno-associated viruses (AAV) serotype 9 carrying
579 double-floxed fusion genes for hChR2 (E123A) and EYFP under an EF1a promoter
580 (University of Pennsylvania Vector Core, Addgene #35507) were used to transfect PfN
581 neurons. Injection coordinates were from Bregma: lateral, 0.65 mm; posterior, 2.3 mm; and
582 3.35 mm depth from surface of brain (Rehani et al., 2019). A small hole was bored into the

583 skull with a micro drill bit and a glass pipette was slowly inserted at the PfN coordinates. To
584 minimize backflow, solution was slowly injected; a total volume of 280 nl (>2.5x1012
585 GC/ml) of the AAV constructs was injected over a period of approximately 1.5 min and the
586 pipette was left in place for 5 min before slowly retracting it. Slice physiology experiments
587 were conducted 2-3 weeks after surgery.

588 Slice preparation: Mice were deeply anesthetized with ketamine (200 mg/kg)–xylazine (23.32
589 mg/kg) and perfused transcardially with ice-cold-modified artificial cerebrospinal fluid
590 (ACSF) bubbled with 95% O_2–5% CO_2, and containing (in mM) 2.5 KCl, 26 $NaHCO_3$, 1.25
591 Na2HPO4, 0.5 $CaCl_2$, 10 $MgSO_4$, 0.4 ascorbic acid, 10 glucose and 210 sucrose. The brain
592 was removed, and 275 µm thick sagittal slices containing the striatum were cut in ice-cold-
593 modified ACSF. Slices were then submerged in ACSF, bubbled with 95% O_2–5% CO_2,
594 containing (in mM) 2.5 KCl, 126 NaCl, 26 $NaHCO_3$, 1.25 Na_2HPO_4, 2 $CaCl_2$, 2 $MgSO_4$ and
595 10 glucose, and stored at room temperature for at least 1 h prior to recording.

596 Electrophysiological recording: The slices were transferred to the recording chamber
597 mounted on a Zeiss Axioskop fixed-stage microscope and perfused with oxygenated ACSF at
598 31ºC. During the optogenetic stimulation experiments, in order to guarantee that the effects
599 we measured were generated post-synaptically, the ACSF solution contained (in µM) 10
600 DNQX to block AMPA receptors, 50 D-APV to block NMDA receptors, 10 gabazine
601 (SR95531) to block $GABA_A$ receptors, and 2 CGP55845 to block $GABA_B$ receptors. An
602 Olympus 60X, 0.9 NA water-immersion objective with a 26.5 mm field number (FN) was
603 used to examine the slice using standard infrared differential interference contrast video
604 microscopy. Patch pipette resistance was typically 4-5 MΩ when filled with recording
605 solutions. The junction potential estimated at 7-8 mV was not corrected. The intracellular
606 solution contained (in mM) 135.5 KCH_3SO_3, 5 KCl, 2.5 NaCl, 5 Na-phosphocreatine, 10
607 HEPES, 0.2 EGTA, 0.21 Na_2GTP, and 2 $Mg_{1.5}ATP$, pH 7.3 with KOH (280–290 mOsm/kg).
608 In the Ca^{2+} imaging experiments (see below) the internal solution contained (in mM) 135 K-
609 gluconate, 5 KCl, 2.5 NaCl, 5 Na-phosphocreatine, 10 HEPES, 0.1 fluo-4 (Molecular
610 Probes), 0.1 Alexa Fluor 568 (for morphological visualization, Molecular Probes), 0.21
611 Na_2GTP, and 2 $Mg_{1.5}ATP$, pH 7.3 with KOH (280–290 mOsm/kg). Electrophysiological
612 recordings were obtained with a MultiClamp 700B amplifier (Molecular Devices, Sunnyvale,
613 CA). Signals were filtered at 10 kHz online, digitized at 10 or 20 kHz and logged onto a
614 personal computer with the Signal 6 software (Cambridge Electronic Design, Cambridge,

615 UK). All reagents, drugs and toxins were purchased from either Merck/Sigma-Aldrich
616 (Darmstadt, Germany), Tocris Biosciences (Bristol, UK) or HelloBio (Bristol, UK).

617 Voltage-perturbation experiments: CINs were held at either –55 mV or –70 mV and were
618 given an 83 second-long voltage command structured as a concatenated sequence of
619 sinusoids from a discrete set of frequencies ranging from 0.2 to 20 Hz with an amplitude of 2
620 mV (3 or 5 seconds per frequency, such that each frequency was represented by an integer
621 multiple of its fundamental period). Phase shifts between the voltage sinusoidal and the
622 somatic current response were determined by the location of the peak in the cross-correlation
623 function (CCF) of the two traces (whose units are mV·pA), for each stimulation frequency
624 and for each illumination condition. The impedance at each frequency, $|Z(f)|$, was calculated
625 from the maximal amplitude of the CCF as $|Z(f)| = (2\ \text{mV})^2/\max(\text{CCF})$ (so that its units are
626 GΩ).

627 Optogenetic stimulation: Optogenetic stimulation was performed with blue-light (470 nm)
628 LED illumination via the objective (Mightex, Toronto, ON, Canada). We used two spatial
629 illumination regimes: a) *proximal illumination* wherein an opaque disk with a central pinhole
630 was placed in the back focal plane of the 60X water-immersion objective such that a ~130
631 μm diameter region around the soma was illuminated (Tiroshi and Goldberg, 2019), thereby
632 targeting the soma and proximal dendrites; and b) *full-field illumination* of the entire slice
633 with a 5X air objective which excites the soma and the entire dendritic field. In all
634 experiments, LED light intensity was chosen such that stimulation generated comparable
635 current responses for both regimes. We used the same sequence of sinusoids described above,
636 only this time the voltage driving the LED was modulated (the minimal voltage was the
637 LED's voltage threshold, 40 mV). The phase delays were again calculated according to the
638 latency of the peak of the CCF between the LED voltage command and somatic current.
639 Note, that the phases were corrected by 0.5 (or by π in radians) due to the fact that the ChR2
640 inward current is in antiphase with the LED's voltage command.

641 Two-photon laser scanning microscopy (2PLSM): The two-photon excitation source was a
642 Chameleon Vision II tunable Ti:Sapphire pulsed laser (Coherent, Santa Clara, CA, USA)
643 tuned to 820 nm. The images were collected with the Femto2D system (Femtonics, Budapest,
644 Hungary) which includes two 3 mm galvo-scanners, one gated GaAsP and one multi-alkaline
645 non-descanned photomultiplier tube for imaging fluo-4 and Alexa Fluor, respectively. Z-
646 stacks of optical sections (spaced 2 μm apart) were collected using 0.2 μm pixels and 15 μs

dwell times. Optical and electrophysiological data were obtained using the software package MES (Femtonics), which also integrates the control of all hardware units in the microscope. The software automates and synchronizes the imaging signals and electrophysiological protocols. Data was extracted from the MES package to personal computers using custom-made code in MATLAB. We recorded spontaneously occurring bAPs with line scans at various distances measured radially from the tip of the soma. Spike triggered averages of the calcium measurements ($\Delta F/F_0$) were estimated and an alpha-function was fit to them. The value of the peak of the fitted alpha-function was used as a measure of the size of the spontaneous bAP at that location.

Drugs and Reagents: TTX was used to block voltage-activated Na^+ currents. Ranolazine was used to block NaP. ZD7288 was used to block the HCN current. Gabazine (SR-95531) and CGP 55845 were used to block $GABA_A$ and $GABA_B$ receptors, respectively. All reagents, drugs and toxins were purchased from either Merck/Sigma-Aldrich (Darmstadt, Germany), Tocris Biosciences (Bristol, UK) or HelloBio (Bristol, UK).

Data analysis and statistics: Data were analyzed and curve fitting was performed using custom code in Matlab (MathWorks, Natick, MA, USA).

Parameter fitting to the phase delay: In our previous study (Tiroshi and Goldberg, 2019), we modeled the dendritic arbor as a semi-infinite cable with a homogeneous quasi-linear membrane (i.e., the current density of each nonlinearity is constant along the dendrite). When a segment of length r (measured in units of the dendrite's space constant) from the soma is activated with a sinusoidal current injection (to model the 470 nm illumination of the ChR2-laden dendrites, which activates the inward current carried by the ChR2), the dendritic phase delay is given by

$$\phi_d = \frac{1}{2\pi}\left(\tan^{-1}\frac{q}{p} - \tan^{-1}\frac{\sin qr}{e^{pr} - \cos qr}\right) \qquad \text{(Eq. 1)}$$

where

$$p = \sqrt{\frac{\sqrt{\alpha^2+\beta^2}+\alpha}{2}} \qquad q = \sqrt{\frac{\sqrt{\alpha^2+\beta^2}-\alpha}{2}} \qquad \text{(Eq. 2)}$$

α and β are functions of frequency and are determined by the linearization of the dendritic nonlinearities as explained in Goldberg et al. (2007) and Remme and Rinzel (2011), with a negative amplifying parameter, μ_n, and a positive resonance parameter, μ_h.

$$\alpha(f) = \gamma_R + \frac{\mu_n}{1 + (2\pi f \tau_n)^2} + \frac{\mu_h}{1 + (2\pi f \tau_h)^2} \qquad \text{(Eq. 3a)}$$

$$\beta(f) = 2\pi f \left[\tau - \frac{\mu_n \tau_n}{1 + (2\pi f \tau_n)^2} - \frac{\mu_h \tau_h}{1 + (2\pi f \tau_h)^2}\right] \qquad \text{(Eq. 3b)}$$

Additional parameters include total dendritic conductance (relative to leak), γ_R, the membrane time constant τ, and the time constants representing the kinetics of the nonlinear dendritic conductances, as explained in Goldberg et al. (2007) and Remme and Rinzel (2011). In some cases we only used the amplifying parameter in the fit (e.g., Fig. 1C).

Using the same formalism it is easy to show that for the (isopotential) soma with a quasi-linear membrane the phase delay is given by

$$\phi_s = \frac{1}{2\pi} \tan^{-1} \frac{\beta}{\alpha} \qquad \text{(Eq. 4)}$$

corresponding to an amplitude that is equal to $(\alpha^2 + \beta^2)^{-1/2}$ up to a scaling factor. In the main text, we point out that when μ_n becomes less negative ϕ_s is reduced. This is because when μ_n becomes less negative α is increased (Eq. 3a) and β is decreased (Eq. 3b). Thus, when we fit only somatic delays we use ϕ_s, but when we fit the dendritic delays we use the sum of $\phi_s + \phi_d$, because the dendritic perturbation as recorded by the intracellular electrode is filtered both by the dendritic and the somatic (quasi-linear) membranes.

Statistics: Null hypotheses were rejected if the P-value was below 0.05. The nonparametric two-tailed Wilcoxon signed-rank test was used for matched samples and the Wilcoxon rank-sum test was used for independent samples. The parametric ANCOVA test was used to test significant changes in the amplitude and phase curves as a function of the natural logarithm of the frequencies (an operation which spreads out this independent parameter more uniformly). Null hypotheses were rejected if the P-value was below 0.05.

For the TAN and SPN locking to slow wave peak analysis, confidence intervals (at P-value of 0.01) were calculated based on the distribution of conditional firing rates 1 s before and after the slow wave peak.

Acknowledgments

This work was funded by a European Research Council (ERC) Consolidator Grant (no. 646886) to J.A.G. and grants from the Israel Science Foundation (no. 2051/20), German Research Foundation (CRC TRR295), Israel-China Binational Science Foundation and the Silverstein Foundation to H.B. We would like to thank Ronit Cherki and Anatoly Shapochnikov for excellent technical assistance.

Competing interests

The authors declare no competing interests.

References

Abudukeyoumu N, Hernandez-Flores T, Garcia-Munoz M, Arbuthnott GW. 2019. Cholinergic modulation of striatal microcircuits. *Eur J Neurosci* **49**:604–622. doi:10.1111/ejn.13949

Aceves Buendia J de J, Tiroshi L, Chiu W, Goldberg JA. 2019. Selective remodeling of glutamatergic transmission to striatal cholinergic interneurons after dopamine depletion. *Eur J Neurosci* **49**:824–833. doi:10.1111/ejn.13715

Alzheimer C, Schwindt P, Crill W. 1993. Modal gating of Na+ channels as a mechanism of persistent Na+ current in pyramidal neurons from rat and cat sensorimotor cortex. *J Neurosci* **13**:660–673. doi:10.1523/JNEUROSCI.13-02-00660.1993

Aoki S, Liu AW, Akamine Y, Zucca A, Zucca S, Wickens JR. 2018. Cholinergic interneurons in the rat striatum modulate substitution of habits. *Eur J Neurosci* **47**:1194–1205. doi:10.1111/ejn.13820

Aosaki T, Kimura M, Graybiel AM. 1995. Temporal and spatial characteristics of tonically active neurons of the primate's striatum. *J Neurophysiol* **73**:1234–1252.

Aosaki T, Tsubokawa H, Ishida A, Watanabe K, Graybiel AM, Kimura M. 1994. Responses of tonically active neurons in the primate's striatum undergo systematic changes during behavioral sensorimotor conditioning. *J Neurosci* **14**:3969–3984.

Apicella P, Scarnati E, Schultz W. 1991. Tonically discharging neurons of monkey striatum respond to preparatory and rewarding stimuli. *Exp Brain Res* **84**:672–675.

Arenkiel BR, Peca J, Davison IG, Feliciano C, Deisseroth K, Augustine GJ, Ehlers MD, Feng G. 2007. In vivo light-induced activation of neural circuitry in transgenic mice expressing channelrhodopsin-2. *Neuron* **54**:205–218. doi:10.1016/j.neuron.2007.03.005

Assous M. 2021. Striatal cholinergic transmission. Focus on nicotinic receptors' influence in striatal circuits. *Eur J Neurosci* **53**:2421–2442. doi:10.1111/ejn.15135

Assous M, Kaminer J, Shah F, Garg A, Koós T, Tepper JM. 2017. Differential processing of thalamic information via distinct striatal interneuron circuits. *Nature Communications* **8**:15860. doi:10.1038/ncomms15860

Beatty Joseph A., Song SC, Wilson CJ. 2015. Cell-type-specific resonances shape the responses of striatal neurons to synaptic input. *Journal of Neurophysiology* **113**:688–700. doi:10.1152/jn.00827.2014

Bennett BD, Callaway JC, Wilson CJ. 2000. Intrinsic membrane properties underlying spontaneous tonic firing in neostriatal cholinergic interneurons. *J Neurosci* **20**:8493–8503. doi:20/22/8493 [pii]

Bennett BD, Wilson CJ. 1999. Spontaneous activity of neostriatal cholinergic interneurons in vitro. *J Neurosci* **19**:5586–5596.

Berger T, Larkum ME, Lüscher H-R. 2001. High I_h Channel Density in the Distal Apical Dendrite of Layer V Pyramidal Cells Increases Bidirectional Attenuation of EPSPs. *Journal of Neurophysiology* **85**:855–868. doi:10.1152/jn.2001.85.2.855

Bradfield LA, Bertran-Gonzalez J, Chieng B, Balleine BW. 2013. The Thalamostriatal Pathway and Cholinergic Control of Goal-Directed Action: Interlacing New with Existing Learning in the Striatum. *Neuron* **79**:153–166. doi:10.1016/j.neuron.2013.04.039

Brown RE, Basheer R, McKenna JT, Strecker RE, McCarley RW. 2012. Control of Sleep and Wakefulness. *Physiological Reviews* **92**:1087–1187. doi:10.1152/physrev.00032.2011

Buzsáki G, Anastassiou CA, Koch C. 2012. The origin of extracellular fields and currents — EEG, ECoG, LFP and spikes. *Nat Rev Neurosci* **13**:407–420. doi:10.1038/nrn3241

Carter AG, Sabatini BL. 2004. State-Dependent Calcium Signaling in Dendritic Spines of Striatal Medium Spiny Neurons. *Neuron* **44**:483–493. doi:10.1016/j.neuron.2004.10.013

Choi SJ, Ma TC, Ding Y, Cheung T, Joshi N, Sulzer D, Mosharov EV, Kang UJ. 2020. Alterations in the intrinsic properties of striatal cholinergic interneurons after dopamine lesion and chronic L-DOPA. *eLife* **9**:e56920. doi:10.7554/eLife.56920

Day M, Wokosin D, Plotkin JL, Tian X, Surmeier DJ. 2008. Differential Excitability and Modulation of Striatal Medium Spiny Neuron Dendrites. *Journal of Neuroscience* **28**:11603–11614. doi:10.1523/JNEUROSCI.1840-08.2008

Deng P, Zhang Y, Xu ZC. 2007. Involvement of I(h) in dopamine modulation of tonic firing in striatal cholinergic interneurons. *J Neurosci* **27**:3148–3156. doi:27/12/3148 [pii] 10.1523/JNEUROSCI.5535-06.2007

Deng YP, Wong T, Bricker-Anthony C, Deng B, Reiner A. 2013. Loss of corticostriatal and thalamostriatal synaptic terminals precedes striatal projection neuron pathology in heterozygous Q140 Huntington's disease mice. *Neurobiol Dis* **60**:89–107. doi:10.1016/j.nbd.2013.08.009

Ding J, Guzman JN, Tkatch T, Chen S, Goldberg JA, Ebert PJ, Levitt P, Wilson CJ, Hamm HE, Surmeier DJ. 2006. RGS4-dependent attenuation of M4 autoreceptor function in striatal cholinergic interneurons following dopamine depletion. *Nat Neurosci* **9**:832–842. doi:10.1038/nn1700

Ding JB, Guzman JN, Peterson JD, Goldberg JA, Surmeier DJ. 2010. Thalamic Gating of Corticostriatal Signaling by Cholinergic Interneurons. *Neuron* **67**:294–307. doi:10.1016/j.neuron.2010.06.017

Ding Y, Won L, Britt JP, Lim SAO, McGehee DS, Kang UJ. 2011. Enhanced striatal cholinergic neuronal activity mediates L-DOPA-induced dyskinesia in parkinsonian mice. *Proceedings of the National Academy of Sciences* **108**:840–845. doi:10.1073/pnas.1006511108

Doig NM, Magill PJ, Apicella P, Bolam JP, Sharott A. 2014. Cortical and Thalamic Excitation Mediate the Multiphasic Responses of Striatal Cholinergic Interneurons to Motivationally Salient Stimuli. *Journal of Neuroscience* **34**:3101–3117. doi:10.1523/JNEUROSCI.4627-13.2014

Eskow Jaunarajs KL, Bonsi P, Chesselet MF, Standaert DG, Pisani A. 2015. Striatal cholinergic dysfunction as a unifying theme in the pathophysiology of dystonia. *Progress in Neurobiology* **127–128**:91–107. doi:10.1016/j.pneurobio.2015.02.002

Goldberg JA, Deister CA, Wilson CJ. 2007. Response Properties and Synchronization of Rhythmically Firing Dendritic Neurons. *Journal of Neurophysiology* **97**:208–219. doi:10.1152/jn.00810.2006

Goldberg JA, Ding JB, Surmeier DJ. 2012. Muscarinic Modulation of Striatal Function and Circuitry In: Fryer AD, Christopoulos A, Nathanson NM, editors. Muscarinic Receptors, Handbook of Experimental Pharmacology. Berlin, Heidelberg: Springer Berlin Heidelberg. pp. 223–241. doi:10.1007/978-3-642-23274-9_10

Goldberg JA, Reynolds JN. 2011. Spontaneous firing and evoked pauses in the tonically active cholinergic interneurons of the striatum. *Neuroscience* **198**:27–43. doi:10.1016/j.neuroscience.2011.08.067

Goldberg JA, Teagarden MA, Foehring RC, Wilson CJ. 2009. Nonequilibrium Calcium Dynamics Regulate the Autonomous Firing Pattern of Rat Striatal Cholinergic Interneurons. *Journal of Neuroscience* **29**:8396–8407. doi:10.1523/JNEUROSCI.5582-08.2009

Goldberg JA, Wilson CJ. 2010. The Cholinergic Interneurons of the Striatum: Intrinsic Properties Underlie Multiple Discharge Patterns. In: Steiner H, Tseng KY, editors. Handbook of Basal Ganglia Structure and Function. London: Academic Press. pp. 133–149.

Goldberg JA, Wilson CJ. 2005. Control of Spontaneous Firing Patterns by the Selective Coupling of Calcium Currents to Calcium-Activated Potassium Currents in Striatal Cholinergic Interneurons. *Journal of Neuroscience* **25**:10230–10238. doi:10.1523/JNEUROSCI.2734-05.2005

Graybiel A, Aosaki T, Flaherty A, Kimura M. 1994. The basal ganglia and adaptive motor control. *Science* **265**:1826–1831. doi:10.1126/science.8091209

Gritton HJ, Howe WM, Romano MF, DiFeliceantonio AG, Kramer MA, Saligrama V, Bucklin ME, Zemel D, Han X. 2019. Unique contributions of parvalbumin and cholinergic interneurons in organizing striatal networks during movement. *Nat Neurosci* **22**:586–597. doi:10.1038/s41593-019-0341-3

Häusser M. 2021. Optogenetics — The Might of Light. *N Engl J Med* **385**:1623–1626. doi:10.1056/NEJMcibr2111915

Helseth AR, Hernandez-Martinez R, Hall VL, Oliver ML, Turner BD, Caffall ZF, Rittiner JE, Shipman MK, King CS, Gradinaru V, Gerfen C, Costa-Mattioli M, Calakos N. 2021. Cholinergic neurons constitutively engage the ISR for dopamine modulation and skill learning in mice. *Science* **372**:eabe1931. doi:10.1126/science.abe1931

Higgs MH, Wilson CJ. 2017. Measurement of phase resetting curves using optogenetic barrage stimuli. *Journal of Neuroscience Methods* **289**:23–30. doi:10.1016/j.jneumeth.2017.06.018

Howe M, Ridouh I, Allegra Mascaro AL, Larios A, Azcorra M, Dombeck DA. 2019. Coordination of rapid cholinergic and dopaminergic signaling in striatum during spontaneous movement. *eLife* **8**:e44903. doi:10.7554/eLife.44903

Hutcheon B, Miura RM, Puil E. 1996. Subthreshold membrane resonance in neocortical neurons. *Journal of Neurophysiology* **76**:683–697. doi:10.1152/jn.1996.76.2.683

Hutcheon B, Yarom Y. 2000. Resonance, oscillation and the intrinsic frequency preferences of neurons. *Trends in Neurosciences* **23**:216–222. doi:10.1016/S0166-2236(00)01547-2

Johansson Y, Silberberg G. 2020. The Functional Organization of Cortical and Thalamic Inputs onto Five Types of Striatal Neurons Is Determined by Source and Target Cell Identities. *Cell Reports* **30**:1178-1194.e3. doi:10.1016/j.celrep.2019.12.095

Joshua M, Adler A, Mitelman R, Vaadia E, Bergman H. 2008. Midbrain Dopaminergic Neurons and Striatal Cholinergic Interneurons Encode the Difference between Reward and Aversive Events at Different Epochs of Probabilistic Classical Conditioning Trials. *Journal of Neuroscience* **28**:11673–11684. doi:10.1523/JNEUROSCI.3839-08.2008

Kawaguchi Y. 1993. Physiological, morphological, and histochemical characterization of three classes of interneurons in rat neostriatum. *J Neurosci* **13**:4908–4923. doi:10.1523/JNEUROSCI.13-11-04908.1993

Kerr JND. 2004. Action Potential Timing Determines Dendritic Calcium during Striatal Up-States. *Journal of Neuroscience* **24**:877–885. doi:10.1523/JNEUROSCI.4475-03.2004

Kim CK, Adhikari A, Deisseroth K. 2017. Integration of optogenetics with complementary methodologies in systems neuroscience. *Nat Rev Neurosci* **18**:222–235. doi:10.1038/nrn.2017.15

Kimura M, Rajkowski J, Evarts E. 1984. Tonically discharging putamen neurons exhibit set-dependent responses. *Proceedings of the National Academy of Sciences* **81**:4998–5001. doi:10.1073/pnas.81.15.4998

Koch C. 1984. Cable theory in neurons with active, linearized membranes. *Biol Cybern* **50**:15–33. doi:10.1007/BF00317936

Kosillo P, Zhang Y-F, Threlfell S, Cragg SJ. 2016. Cortical Control of Striatal Dopamine Transmission via Striatal Cholinergic Interneurons. *Cereb Cortex* **26**:4160–4169. doi:10.1093/cercor/bhw252

Lapper SR, Bolam JP. 1992. Input From the Frontal Cortex and the Nucleus To Cholinergic Interneurons in the Dorsal of the Rat **51**:533–545.

Liu D, Dan Y. 2019. A Motor Theory of Sleep-Wake Control: Arousal-Action Circuit. *Annu Rev Neurosci* **42**:27–46. doi:10.1146/annurev-neuro-080317-061813

Mallet N, Leblois A, Maurice N, Beurrier C. 2019. Striatal Cholinergic Interneurons: How to Elucidate Their Function in Health and Disease. *Front Pharmacol* **10**:1488. doi:10.3389/fphar.2019.01488

Martin RF, Bowden DM. 2000. Primate brain maps: structure of the macaque brain. Elsevier.

Matsumoto N, Minamimoto T, Graybiel AM, Kimura M. 2001. Neurons in the Thalamic CM-Pf Complex Supply Striatal Neurons With Information About Behaviorally Significant Sensory Events. *Journal of Neurophysiology* **85**:960–976. doi:10.1152/jn.2001.85.2.960

Maurice N. 2004. D2 Dopamine Receptor-Mediated Modulation of Voltage-Dependent Na+ Channels Reduces Autonomous Activity in Striatal Cholinergic Interneurons. *Journal of Neuroscience* **24**:10289–10301. doi:10.1523/JNEUROSCI.2155-04.2004

Mauro A, Conti F, Dodge F, Schor R. 1970. Subthreshold Behavior and Phenomenological Impedance of the Squid Giant Axon. *Journal of General Physiology* **55**:497–523. doi:10.1085/jgp.55.4.497

McGuirt AF, Post MR, Pigulevskiy I, Sulzer D, Lieberman OJ. 2021. Coordinated Postnatal Maturation of Striatal Cholinergic Interneurons and Dopamine Release Dynamics in Mice. *J Neurosci* **41**:3597–3609. doi:10.1523/JNEUROSCI.0755-20.2021

Mizrahi-Kliger AD, Kaplan A, Israel Z, Bergman H. 2018. Desynchronization of slow oscillations in the basal ganglia during natural sleep. *Proc Natl Acad Sci USA* **115**:E4274–E4283. doi:10.1073/pnas.1720795115

Morris G, Arkadir D, Nevet A, Vaadia E, Bergman H. 2004. Coincident but distinct messages of midbrain dopamine and striatal tonically active neurons. *Neuron* **43**:133–143. doi:10.1016/j.neuron.2004.06.012 S0896627304003551 [pii]

Oswald MJ, Oorschot DE, Schulz JM, Lipski J, Reynolds JN. 2009. IH current generates the afterhyperpolarisation following activation of subthreshold cortical synaptic inputs to striatal cholinergic interneurons. *J Physiol* **587**:5879–5897. doi:jphysiol.2009.177600 [pii] 10.1113/jphysiol.2009.177600

Parker PRL, Lalive AL, Kreitzer AC. 2016. Pathway-Specific Remodeling of Thalamostriatal Synapses in Parkinsonian Mice. *Neuron* **89**:734–740. doi:10.1016/j.neuron.2015.12.038

Paz RM, Tubert C, Stahl AM, Amarillo Y, Rela L, Murer MG. 2021. Levodopa Causes Striatal Cholinergic Interneuron Burst-Pause Activity in Parkinsonian Mice. *Mov Disord* **36**:1578–1591. doi:10.1002/mds.28516

Pisani A, Bernardi G, Ding J, Surmeier DJ. 2007. Re-emergence of striatal cholinergic interneurons in movement disorders. *Trends in Neurosciences* **30**:545–553. doi:10.1016/j.tins.2007.07.008

Plotkin JL, Goldberg JA. 2019. Thinking Outside the Box (and Arrow): Current Themes in Striatal Dysfunction in Movement Disorders. *Neuroscientist* **25**:359–379. doi:10.1177/1073858418807887

Poppi LA, Ho-Nguyen KT, Shi A, Daut CT, Tischfield MA. 2021. Recurrent Implication of Striatal Cholinergic Interneurons in a Range of Neurodevelopmental, Neurodegenerative, and Neuropsychiatric Disorders. *Cells* **10**:907. doi:10.3390/cells10040907

Raz A, Feingold A, Zelanskaya V, Vaadia E, Bergman H. 1996. Neuronal synchronization of tonically active neurons in the striatum of normal and parkinsonian primates. *J Neurophysiol* **76**:2083–2088.

Rehani R, Atamna Y, Tiroshi L, Chiu W-H, de Jesús Aceves Buendía J, Martins GJ, Jacobson GA, Goldberg JA. 2019. Activity Patterns in the Neuropil of Striatal Cholinergic Interneurons in Freely Moving Mice Represent Their Collective Spiking Dynamics. *eNeuro* **6**:ENEURO.0351-18.2018. doi:10.1523/ENEURO.0351-18.2018

Remme MWH, Rinzel J. 2011. Role of active dendritic conductances in subthreshold input integration. *J Comput Neurosci* **31**:13–30. doi:10.1007/s10827-010-0295-7

Riedner BA, Vyazovskiy VV, Huber R, Massimini M, Esser S, Murphy M, Tononi G. 2007. Sleep Homeostasis and Cortical Synchronization: III. A High-Density EEG Study of Sleep Slow Waves in Humans. *Sleep* **30**:1643–1657. doi:10.1093/sleep/30.12.1643

Schulz JM, Oswald MJ, Reynolds JNJ. 2011. Visual-Induced Excitation Leads to Firing Pauses in Striatal Cholinergic Interneurons. *Journal of Neuroscience* **31**:11133–11143. doi:10.1523/JNEUROSCI.0661-11.2011

Schulz JM, Reynolds JNJ. 2013. Pause and rebound: sensory control of cholinergic signaling in the striatum. *Trends in Neurosciences* **36**:41–50. doi:10.1016/j.tins.2012.09.006

Sharott A, Doig NM, Mallet N, Magill PJ. 2012. Relationships between the Firing of Identified Striatal Interneurons and Spontaneous and Driven Cortical Activities In Vivo. *Journal of Neuroscience* **32**:13221–13236. doi:10.1523/JNEUROSCI.2440-12.2012

Smith Y, Raju DV, Pare JF, Sidibe M. 2004. The thalamostriatal system: a highly specific network of the basal ganglia circuitry. *Trends Neurosci* **27**:520–527. doi:10.1016/j.tins.2004.07.004 S0166-2236(04)00232-2 [pii]

Song WJ, Surmeier DJ. 1996. Voltage-dependent facilitation of calcium channels in rat neostriatal neurons. *J Neurophysiol* **76**:2290–2306.

Tanimura A, Du Y, Kondapalli J, Wokosin DL, Surmeier DJ. 2019. Cholinergic Interneurons Amplify Thalamostriatal Excitation of Striatal Indirect Pathway Neurons in Parkinson's Disease Models. *Neuron* **101**:444-458.e6. doi:10.1016/j.neuron.2018.12.004

Tanimura A, Lim SAO, Aceves Buendia J de J, Goldberg JA, Surmeier DJ. 2016. Cholinergic Interneurons Amplify Corticostriatal Synaptic Responses in the Q175 Model of Huntington's Disease. *Front Syst Neurosci* **10**. doi:10.3389/fnsys.2016.00102

Thomas TM, Smith Y, Levey AI, Hersch SM. 2000. Cortical Inputs to m2-Immunoreactive Striatal Interneurons in Rat and Monkey. *Synapse* **37**:252–261.

Thorn CA, Graybiel AM. 2010. Pausing to Regroup: Thalamic Gating of Cortico-Basal Ganglia Networks. *Neuron* **67**:175–178. doi:10.1016/j.neuron.2010.07.010

Threlfell S, Lalic T, Platt NJ, Jennings KA, Deisseroth K, Cragg SJ. 2012. Striatal Dopamine Release Is Triggered by Synchronized Activity in Cholinergic Interneurons. *Neuron* **75**:58–64. doi:10.1016/j.neuron.2012.04.038

Tiroshi L, Goldberg JA. 2019. Population dynamics and entrainment of basal ganglia pacemakers are shaped by their dendritic arbors. *PLoS Comput Biol* **15**:e1006782. doi:10.1371/journal.pcbi.1006782

Tubert C, Murer MG. 2021. What's wrong with the striatal cholinergic interneurons in Parkinson's disease? Focus on intrinsic excitability. *Eur J Neurosci* **53**:2100–2116. doi:10.1111/ejn.14742

Ulrich D. 2002. Dendritic Resonance in Rat Neocortical Pyramidal Cells. *Journal of Neurophysiology* **87**:2753–2759. doi:10.1152/jn.2002.87.6.2753

Wilson C, Chang H, Kitai S. 1990. Firing patterns and synaptic potentials of identified giant aspiny interneurons in the rat neostriatum. *J Neurosci* **10**:508–519. doi:10.1523/JNEUROSCI.10-02-00508.1990

Wilson CJ. 2005. The mechanism of intrinsic amplification of hyperpolarizations and spontaneous bursting in striatal cholinergic interneurons. *Neuron* **45**:575–585.

Wilson CJ. 2004. Basal Ganglia In: Shepherd GM, editor. The Synaptic Organization of the Brain. New York: Oxford University Press. pp. 361–413.

Wilson CJ, Goldberg JA. 2006. Origin of the slow afterhyperpolarization and slow rhythmic bursting in striatal cholinergic interneurons. *J Neurophysiol* **95**:196–204. doi:00630.2005 [pii] 10.1152/jn.00630.2005

Yamanaka K, Hori Y, Minamimoto T, Yamada H, Matsumoto N, Enomoto K, Aosaki T, Graybiel AM, Kimura M. 2018. Roles of centromedian parafascicular nuclei of thalamus and cholinergic interneurons in the dorsal striatum in associative learning of environmental events. *J Neural Transm* **125**:501–513. doi:10.1007/s00702-017-1713-z

Yarom O, Cohen D. 2011. Putative Cholinergic Interneurons in the Ventral and Dorsal Regions of the Striatum Have Distinct Roles in a Two Choice Alternative Association Task. *Front Syst Neurosci* **5**. doi:10.3389/fnsys.2011.00036